THE ASTROPHYSICAL JOURNAL LETTERS, 971:L14 (8pp), 2024 August 10 https://doi.org/10.3847/2041-8213/ad675f

Revisiting the Fundamental Metallicity Relation with Observation and Simulation

Chengyu Ma[1,2], Kai Wang[3,4,5], Enci Wang[1,2], Yingjie Peng[3], Haochen Jiang[1], Haoran Yu[1], Cheng Jia[1], Zeyu Chen[1], Haixin Li[1], and Xu Kong[1,2]

[1] Department of Astronomy, University of Science and Technology of China, Hefei 230026, People's Republic of China; ecwang16@ustc.edu.cn
[2] School of Astronomy and Space Science, University of Science and Technology of China, Hefei 230026, People's Republic of China
[3] Kavli Institute for Astronomy and Astrophysics, Peking University, Beijing 100871, People's Republic of China; wkcosmology@gmail.com
[4] Institute for Computational Cosmology, Department of Physics, Durham University, South Road, Durham, DH1 3LE, UK
[5] Centre for Extragalactic Astronomy, Department of Physics, Durham University, South Road, Durham, DH1 3LE, UK
Received 2024 July 1; revised 2024 July 23; accepted 2024 July 24; published 2024 August 6

Abstract

The gas-phase metallicity of galaxies is regulated by multiple astrophysical processes, which makes it a crucial diagnostic of galaxy formation and evolution. Beyond the fundamental mass–metallicity relation, a debate about the secondary galaxy property to predict the metallicity of galaxies arises. Motivated by this, we systematically examine the relationship between gas-phase metallicity and other galaxy properties, i.e., the star formation rate (SFR) and galaxy size, in addition to stellar mass in both observation and simulation. We utilize the data from the Mapping Nearby Galaxies at Apache Point Observatory survey and the TNG50 simulations. We find that the combination of M_*/R_e^β with $\beta \sim 0.6$–1 is in much stronger correlation to the metallicity than stellar mass alone, regardless of whether the SFR is included or not, in both observation and simulation. This indicates that galaxy size plays a more important role in determining gas-phase metallicity of galaxies than SFR. In addition, The Next Generation simulation predicts that the SFR, although being a subdominant role, becomes increasingly important in the high-z universe. Finally, we speculate that the SFR modulates metallicity on the temporal dimension, synchronized with time-varying gas inflows, and galaxy size regulates metallicity on the spatial dimension by affecting the gravitational potential and the mass-loading factor.

Unified Astronomy Thesaurus concepts: Metallicity (1031); Galaxy evolution (594); Galaxy chemical evolution (580)

1. Introduction

Galaxy formation and evolution are regulated by multiple astrophysical processes, including gas cooling and accretion, star formation, stellar and AGN feedback and associated gas outflows, the recycling of the ejected gas, and others (e.g., Bouché et al. 2010; Schaye et al. 2010; Davé et al. 2011; Lilly et al. 2013; Peng & Maiolino 2014; Belfiore et al. 2019; Wang et al. 2019; Wang & Lilly 2021, 2022; Wang et al. 2023b). Each of these processes leaves their signature on the metal content of galaxies, which, in turn, makes metallicity a crucial diagnostic of these physical processes during galaxy formation and evolution. However, due to the complexity of the situation, it is unpractical to directly infer the role played by each individual physical process from the metal content of the galaxy. Instead, we first establish the scaling relations between the metal content and other galaxy properties and comprehend these scaling relations with the facility of semianalytical models and numerical simulations, which has already become a common practice.

The most fundamental scaling relation is the mass–metallicity relation (MZR; e.g., Lequeux et al. 1979; Tremonti et al. 2004), which says that gas in massive galaxies is more metal enriched than that in low-mass galaxies. Specifically, based on large numbers of galaxies from the Sloan Digital Sky Survey (SDSS; Stoughton et al. 2002), Tremonti et al. (2004) found a strong correlation between stellar mass and gas-phase metallicity for star-forming galaxies, which is referred to as the MZR. MZR is also established at high z, but the overall amplitude decreases with increasing redshift, which indicates that high-z galaxies are more metal poor compared to their low-z counterparts at fixed stellar mass (e.g., Savaglio et al. 2005; Maier et al. 2006; Maiolino et al. 2008). The correlation between stellar mass and gas-phase metallicity can be driven by several factors, including outflows driven by supernova winds (Larson 1974; Finlator & Davé 2008; Bassini et al. 2024) and varying star formation efficiencies in galaxies (Brooks et al. 2007; Calura et al. 2009).

Despite the strong correlation between gas-phase metallicity and stellar mass, considerable scatter still remains. Further investigation found that the residual gas-phase metallicity with respect to the mean relation is correlated to the current star formation rate (SFR) of galaxies, and the joint correlation among stellar mass, gas-phase metallicity, and SFR is known as the fundamental metallicity relation (FMR; Lara-López et al. 2010; Mannucci et al. 2010; Richard et al. 2011; Nakajima et al. 2012; Salim et al. 2014; Cresci et al. 2019; Huang et al. 2019; Curti et al. 2020, 2024; Garcia et al. 2024; Pérez-Díaz et al. 2024). In particular, Mannucci et al. (2010) proposed a universal, epoch-independent mass–metallicity–SFR relation. They suggested that the apparent evolution in the MZR could be explained phenomenologically by the redshift evolution of the star-forming main sequence (SFMS). However, recent studies based on deep JWST/NIRSpec spectroscopy found that high-z galaxies, especially $z > 6$, are significantly metal deficient compared with counterparts in the local Universe with controlled stellar mass and SFR (Curti et al. 2024; Pérez-Díaz et al. 2024), which challenges the epoch independency of the FMR.

Recently, growing evidence shows that the gravitational potential of galaxies plays a more fundamental role in regulating the metal content of star-forming galaxies than the stellar mass (e.g., Ellison et al. 2008; D'Eugenio et al. 2018; Sánchez Almeida & Dalla Vecchia 2018; Huang et al. 2019; Sánchez-Menguiano et al. 2024a, 2024b; Ma et al. 2024). A similar conclusion was drawn on the stellar metallicity of galaxies (Barone et al. 2020; Vaughan et al. 2022; Cappellari 2023). These results motivate us to take a closer look at the statistical relationship between gas-phase metallicity and other galaxy properties, which are stellar mass, SFR, and galaxy size in this study, for star-forming galaxies through both observation and simulation, aiming to pin down the fundamental determinant of the metallicity of the gas content in star-forming galaxies. We find consistent results across observations and simulations, which show that stellar mass and galaxy size play primary roles, while SFR plays a secondary role in determining the gas-phase metallicity of star-forming galaxies.

This Letter is structured as follows: Section 2 introduces both the observational data and numerical simulations. Section 3 presents our results obtained from the aforementioned data. Finally, Section 4 presents the discussion about the implications on galaxy formation and evolution, together with the summary to our main findings.

2. Data

2.1. Observational Data

The observation sample that we select to research is from Mapping Nearby Galaxies at Apache Point Observatory (MaNGA; Bundy et al. 2015) Data Release 17 (Abdurro'uf et al. 2022). Using the two dual-channel BOSS spectrographs at the Sloan Telescope (Gunn et al. 2006; Smee et al. 2013), MaNGA covers a wavelength of 3600–10300 Å at a resolution of ∼2000. The spatial coverage of individual galaxies is typically larger than 1.5 R_e with a spatial resolution of 1–2 kpc.

The measurements of stellar mass and total SFR are taken from Salim et al. (2018),[6] which are derived from the spectral energy distribution fittings of GALEX, SDSS, and WISE photometry. Based on these two parameters, we derive the SFMS based on the iterative algorithm presented in Wang et al. (2023a; see also Woo et al. 2013; Donnari et al. 2019). We start from an initial guess of the linear function and then iteratively select galaxies within 1 dex of the SFMS and refit the slope and the intercept until convergence. The resulting SFMS is

$$\log\left(\frac{\mathrm{SFR}}{M_\odot \mathrm{yr}^{-1}}\right) = 0.71 \times \log\left(\frac{M_*}{M_\odot}\right) - 7.27. \quad (1)$$

Anchored with this SFMS, we select 5532 star-forming galaxies that lie within 1 dex of this linear function for further analysis in this work.

Since D'Eugenio et al. (2018) found that it is critical to use the aperture-matched metallicity in studying the metallicity scaling relation of galaxies, we in this work use the Hα-luminosity-weighted gas-phase metallicity measured within effective radius (R_e) as a representative of the overall metallicity of MaNGA galaxies (also see Wang & Lilly 2021). The effective radius is measured from the Sérsic fitting on the SDSS r-band image. The gas-phase metallicity of MaNGA galaxies is computed with three methods using different combination of strong lines, which are the `N2S2Hα` diagnostic introduced by Dopita et al. (2016), the `S-calibration` (`Scal` for short) estimator (Pilyugin & Grebel 2016), and the `N2O2` diagnostic (Dopita et al. 2013; Zhang et al. 2017). These three metallicity indicators are particularly adopted due to the following reasons.

The `N2S2Hα` is insensitive to reddening, and Easeman et al. (2024) proposed that `N2S2Hα` is preferred when studying the distribution of metals within galaxies because `N2S2Hα` shows a near-linear relation with Te-based measurement. The `Scal` indicator leverages three emission line ratios, enhancing the accuracy over previous strong-line methods. Pilyugin & Grebel (2016) demonstrated that the `Scal` indicator provides metallicity measurements that closely align with the T_e-based methods, exhibiting a scatter of only approximately 0.05 dex within the metallicity range of $7.0 < 12 + \log(\mathrm{O/H}) < 8.8$. `N2O2` is not sensitive to ionization parameter or ionizing spectrum hardness but to metallicity (Kewley & Dopita 2002; Dopita et al. 2013), while it relies on the N/O. By studying the metallicity of H II regions and diffuse ionized gas (DIG), Zhang et al. (2017) proposed that `N2O2` is optimal among many metallicity indicators in case of the existence of DIG.

2.2. Cosmological Galaxy Formation Simulation

This work employs the state-of-the-art simulation suite of the Illustris The Next Generation (TNG), which comprises several cosmological galaxy formation simulations with different resolutions. Here we use the one with the highest resolution: TNG50 (Nelson et al. 2018; Pillepich et al. 2018). The stellar mass, M_*, and SFR are calculated within twice the effective radius, while the effective radius, R_e, is calibrated so that a sphere with this radius encloses half of the total stellar mass in each subhalo. Here subhalos are identified with the `SUBFIND` algorithm (Springel et al. 2005) using all types of particles in each FoF halo, which is identified using the conventional Friends-of-Friends (FoF) algorithm with only dark matter particles. The gas-phase metallicity, $12 + \log[\mathrm{O/H}]$, is inferred as the ratio between the abundances of oxygen and hydrogen.

For the sake of reliable gas-phase metallicity calculation, we only include galaxies on the SFMS, and this is determined using the iterative algorithm presented in Wang et al. (2023a); the result at $z = 0$ is

$$\log\left(\frac{\mathrm{SFR}}{M_\odot \mathrm{yr}^{-1}}\right) = 0.75 \times \log\left(\frac{M_*}{M_\odot}\right) - 7.72, \quad (2)$$

and we only include galaxies with `SubhaloFlag==1`.

For a fair comparison between observation and simulation, we also need to control the aperture within which all these physical parameters are measured. For stellar mass and SFR, since current cosmological hydrodynamical simulations cannot deliver physical values but rely on the calibration against observational statistics, like stellar mass functions (see the introduction in Schaye et al. 2015), we would better use the aperture used for calibrating the simulation, which is $2R_e$ in all TNG simulations. The gas-phase metallicity is measured within R_e in the observation for the sake of data quality, and we choose to use $2R_e$ in the simulation for physical consistency. In addition, we have checked the results where the gas-phase metallicity was measured within R_e for all simulated galaxies, and it does not impact our scientific conclusions drawn in this work.

[6] https://salims.pages.iu.edu/gswlc/

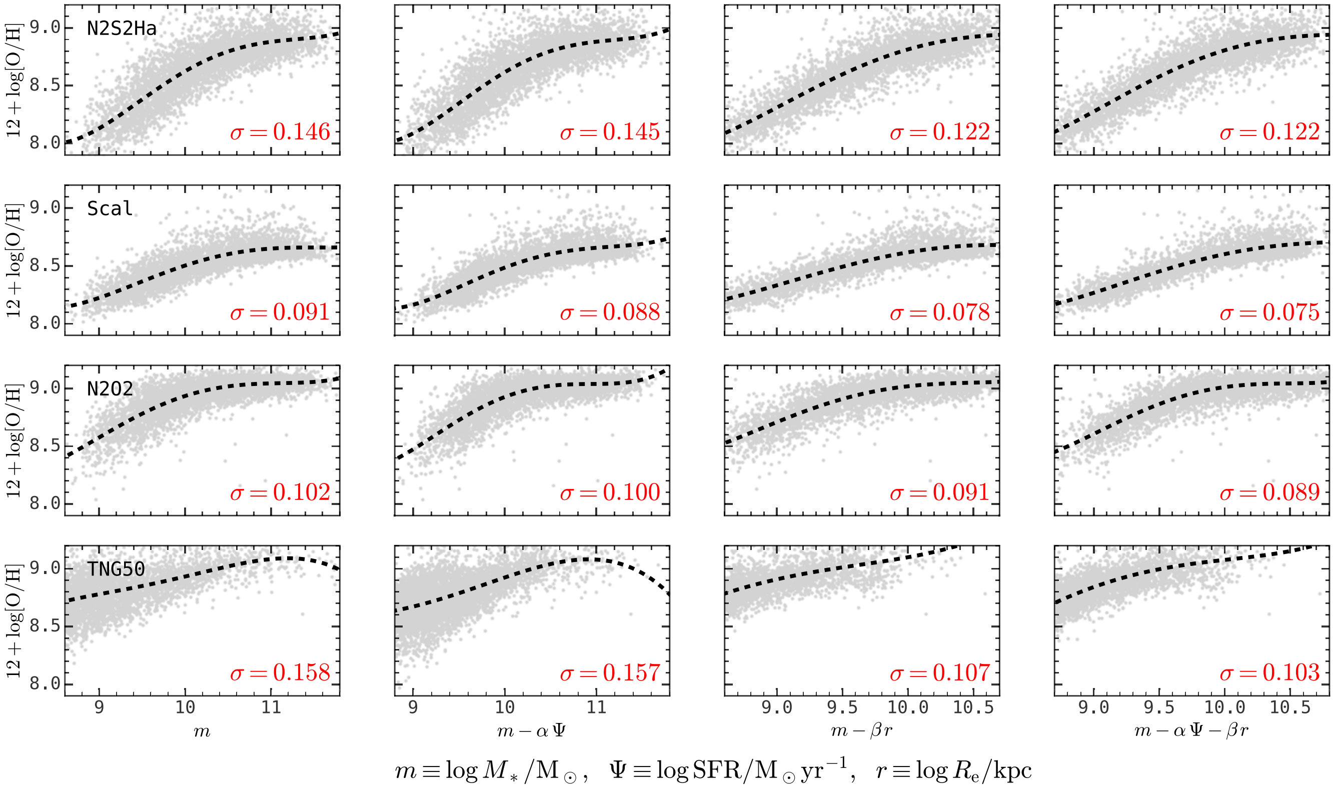

Figure 1. The MZR (first column) of observed galaxies and its relation to SFR (second column), galaxy size (third column), and two quantities combined (forth column). Here three different gas-phase metallicity estimators are used (N2S2Ha, Dopita et al. 2016; Scal, Pilyugin & Grebel 2016). The red text in each panel shows the standard deviation to the fourth-order fitting curve shown in black dashed line, which is denoted as σ. One can see that σ is decreasing from the left panels to right panels. Particularly, the panels of the third column exhibit lower σ compared to those of the second panel, which indicates that galaxy size is a better predictor of the deviation in the MZR compared to SFR.

3. Results

3.1. MZR and Its Relationship to SFR and Size

We design a method to study the relationship among stellar mass, gas-phase metallicity, SFR, and galaxy size for star-forming galaxies. We start from the MZR, as shown on the left panels of Figure 1. First, all three observational metallicity estimators give very similar scaling relations, where the slope is steep at the low-mass end and gradually flattens at the high-mass end, despite the noticeable systematics among the three estimators. Then, we employ a fourth-order polynomial to fit the median relation, and the fitting results are shown in black dashed lines. Finally, we calculate the standard deviation of the gas-phase metallicity with respect to the median relation, which is 0.146/0.091/0.102 for the observational data with different metallicity estimators and 0.158 for TNG50, respectively.

In the second step, we inspect the relationship between the residual on the MZR and the SFR (not shown here), which was found to be fitted by a linear function with the slope as α (e.g., Lara-López et al. 2010; Mannucci et al. 2010; Cresci et al. 2019; Curti et al. 2020, 2024; Pérez-Díaz et al. 2024). The scatter plots of the new variable $\log M_*/M_\odot - \alpha \log \mathrm{SFR}/M_\odot \mathrm{yr}^{-1}$ are shown in the panels on the second column of Figure 1. Again, a fourth-order polynomial was used to fit the median relation, and the standard deviations with respect to this new scaling relation were calculated and labeled on each panel. This step can also proceed in an equivalent way: we start from the correlation between gas-phase metallicity and a new variable, $\log M_*/M_\odot - \alpha \log \mathrm{SFR}/M_\odot \mathrm{yr}^{-1}$, and fit the median relation with a fourth-order polynomial and calculate the standard deviation of the residual. Then, we tune α to minimize the standard deviation.

The standard deviation, σ, calculated on the panels in the second column in Figure 1 must be smaller than the those in the first column, since one additional variable, i.e., SFR, is used to predict the metallicity. Moreover, the decrement of σ reflects the importance of the SFR in predicting gas-phase metallicity, and it is also indicative of the physical causation between the SFR and gas-phase metallicity. Here one can see that, also from Figure 2, that the decrements of the standard deviation in gas-phase metallicity by incorporating the SFR were marginal for all the observational estimators and the TNG50 simulation.

The third step is similar to the second step, except replacing the SFR with galaxy size, R_e. The results are shown in the panels in the third column of Figure 1. Here one can see that the standard deviation, σ, of gas-phase metallicity was significantly reduced by incorporating galaxy size for both observations and the TNG50 simulation, which was more clearly shown in Figure 2.

The final step is to incorporate both the SFR and galaxy size, and the results are presented in the rightmost panels of Figure 1. Here we can see that the standard deviations are very close to the values in the third column (see also Figure 2), which, combined with previous results, indicate that galaxy size plays a more fundamental role in regulating the gas-phase metal content of galaxies in their evolution than the SFR.

Following all four steps above, we can obtain the standard deviations, σ, in four cases, i.e., (M_*), (M_*, SFR), (M_*, R_e), and (M_*, SFR, R_e), and the results are presented in the top panel of Figure 2. Here we can see that the absolute value of

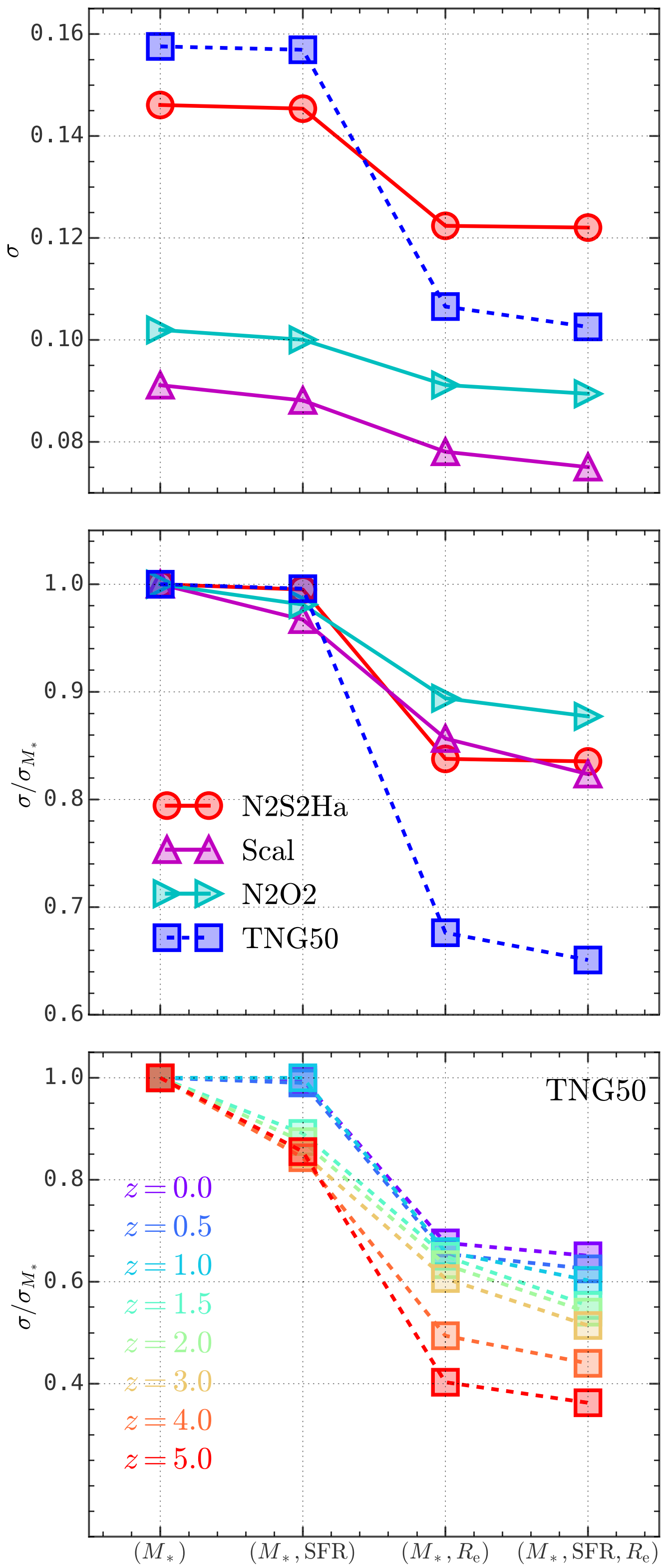

Figure 2. The standard deviation of the residual to the fitting curves in Figure 1 for four different gas-phase metallicity estimators. This figure shows that the inclusion of the SFR only reduces σ by $\lesssim$4%, but the inclusion of R_e can reduce σ by 10%−16%. Besides, including R_e alone can obtain a similar performance to including both R_e and SFR.

standard deviation profoundly depends on the metallicity indicator. `Scal` gives the smallest scatter and `N2S2Ha` gives the largest scatter, while `N2O2` lies in between. Since we only care about the role played by the SFR and galaxy size in reducing the scatter rather than their absolute values, we normalize these scatters using the values obtained with stellar mass alone and proceed to study the decrease by incorporating additional galaxy properties, and the result is presented in the middle panel of Figure 2. Despite the difference in the absolute values of scatters, the normalized scatter behaves quite consistently among the three estimators: incorporating galaxy size can substantially reduce the scatter, while the SFR only plays a minor role. The more intriguing thing is that TNG50 gives rise to qualitatively similar behavior, except that galaxy size plays a more dominating role.

Finally, the best-fitting values of α, β, and (α, β) in the latter three steps are presented in Figure 3. The magenta triangles show the values of α and β when fitted individually with the other parameter sets to zero, and the blue crosses show the results when fitting jointly. The background color renders the σ value as a function of (α, β). The degeneracy between these two parameters is obvious for both observation and simulation, and it comes from the positive correlation between the SFR and galaxy size. Therefore, when only the SFR (galaxy size) is used to fit the residual of the MZR, it can leverage its correlation to galaxy size (SFR) so that the best-fitting α (β) is slightly larger than the value in the joint fitting case. This effect is more strong at high z, as we will see shortly.

3.2. Redshift Evolution in TNG50

The TNG50 simulation enables us to extend this analysis to the high-z universe. As shown in the bottom panel of Figure 2, the galaxy size plays a dominant role in determining the residual of the MZR over the SFR up to $z \sim 5$. Meanwhile, the SFR, although in the subdominant role, becomes increasingly important at high z.

Figure 4 shows the redshift evolution of best-fitting α and β when fitting individually for the SFR and galaxy size and (α, β) when fitting jointly. The rise of α with increasing redshift in both the individual and joint fitting cases supports our claim that the SFR becomes more strongly correlated to the residual in the MZR at high z.

We also note that β increases with redshift when α is set to zero, which trend, however, diminishes when both the SFR and galaxy size are taken into account. Moreover, more importantly, β stays close to unity in the joint fitting case from $z = 0$ to $z \approx 5$. As shown in the Appendix, the ratio between galaxy stellar mass and galaxy size, $\log M_* - \log R_e$, strongly correlates to the gravitational potential at R_e, which is the work that needs to be done by moving a test particle from R_e of the galaxy to the infinity. Our result highlights the necessity of jointly analyzing the dependence of metallicity on the SFR and size. Furthermore, the gravitational potential of galaxies plays a primary role in determining the metallicity of galaxies in TNG50 across the full lifetime of galaxies.

4. Discussion and Summary

4.1. Comparison with Previous Results

Mannucci et al. (2010) studied the relationship between the gas-phase metallicity and SFR of star-forming galaxies, and they found a best-fitting $\alpha \approx 0.32$, which is consistent with our results here. However, they claimed that this coefficient is independent of redshift, while TNG50 predicts that it increases toward higher redshift.

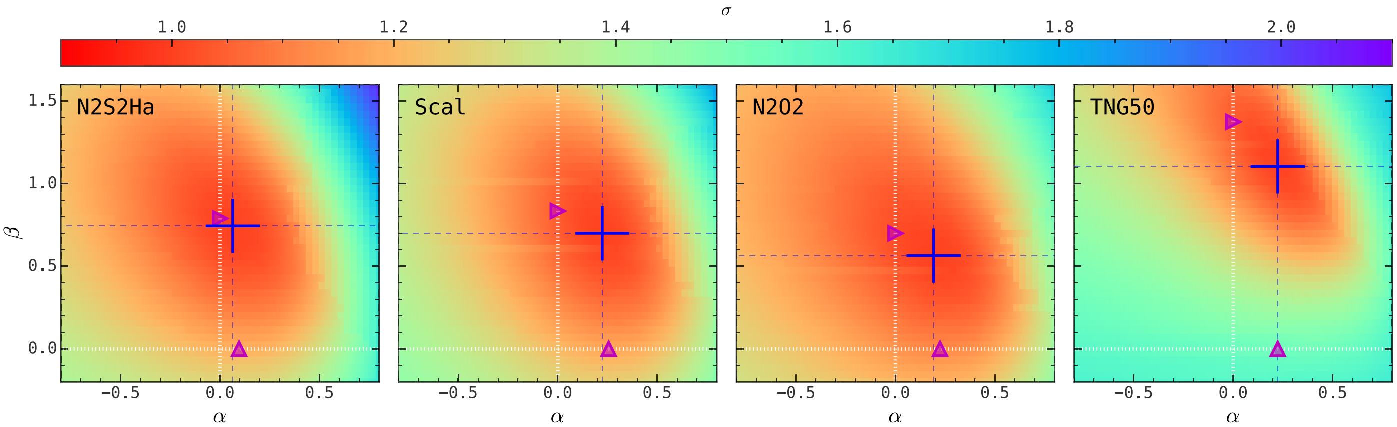

Figure 3. The scatter of the metallicity scaling relations in Figure 1 as a function of the values of α and β for the observations and TNG50. In each panel, the magenta triangles show the values of α and β when fitted individually with the other parameter sets to zero, and the blue crosses show the results when fitting jointly.

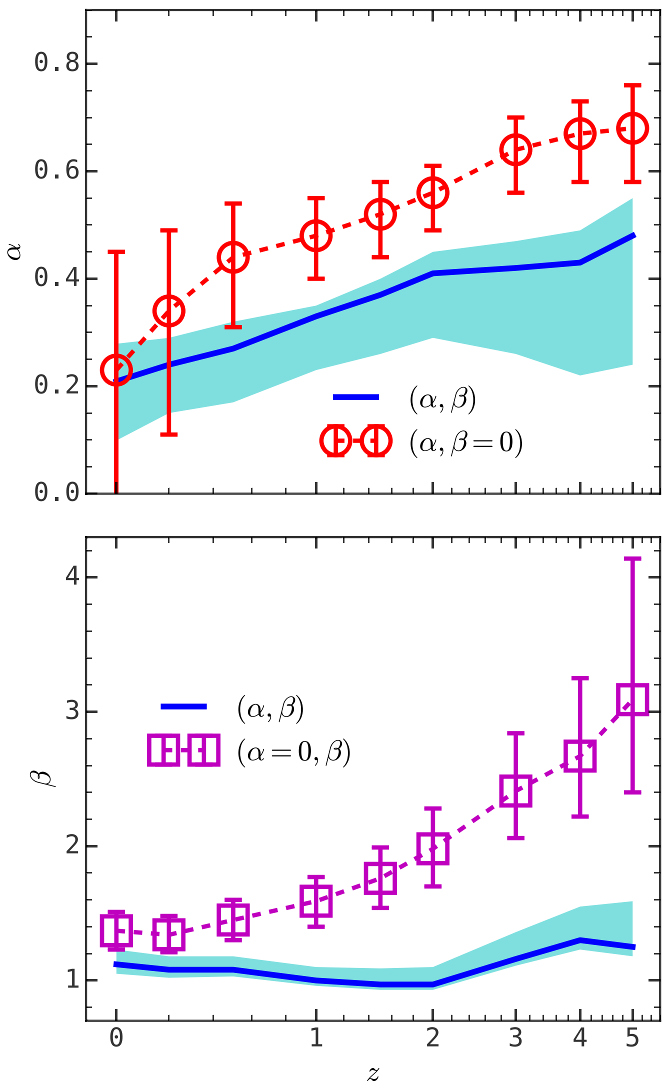

Figure 4. The redshift evolution of best-fitting α and β in TNG50. The red circles in the upper panel show the best-fitting α when β is forced to be zero, and the magenta squares show the best-fitting β when α is forced to be zero. The blue solid lines and cyan shadow regions in both panels show the best-fitting (α, β) when both the SFR and galaxy size are used to fit the residual of the MZR.

D'Eugenio et al. (2018) investigated the correlation between the gas-phase metallicity and effective radius at fixed stellar mass for star-forming galaxies in SDSS DR7. They found these two variables in anticorrelation with the best-fitting slope at about 0.6 for galaxies with $M_* \sim 10^9 M_\odot$, consistent with our results, and the slope flattens to about 0.4 for galaxies with $M_* \sim 10^{10.5} M_\odot$. Similarly, Sánchez-Menguiano et al. (2024b) exhausted 148 galaxy properties to predict the gas-phase metallicity using a random forest regression algorithm, and they found that the compact form of $M_*/R_e^{0.6}$ is able to capture most of the scatter in the gas-phase metallicity, which means that including other properties only improves the performance marginally.

Compared with previous results, our study has several highlights. First, we employ three different metallicity indicators, aiming to the marginalize the inherent systematics of each individual indicator. Second, we simultaneously take the SFR and galaxy size, which are correlated to each other through the mass–size relation, into account to mitigate the risk that one variable takes advantage of their mutual correlation. Finally, we apply the same procedure to simulated galaxies, where the metallicity is calculated directly from element abundance, and obtain qualitatively similar conclusions, which further eliminates the risk that these results are due to observational systematics. Moreover, it supports the modeling of metal-related processes in the TNG simulation.

Furthermore, our study on high-z galaxies in TNG50 predicts that the SFR becomes increasingly important at high z. In addition, the best-fitting α increases with redshift, while the best-fitting β is independent of redshift. These predictions could be tested with upcoming high-z galaxy surveys from Subaru Prime Focus Spectrograph (Takada et al. 2014) and MOONS (Cirasuolo et al. 2014; Maiolino et al. 2020).

4.2. Physical Explanation

In order to understand the scaling relation of metallicity, we consider the metal enrichment process under the gas regulator system (e.g., Schaye et al. 2010; Davé et al. 2011; Lilly et al. 2013; Peng & Maiolino 2014; Wang et al. 2019; Wang & Lilly 2021, 2022), where the instantaneous gas mass is regulated by the interplay of gas inflow, star formation, and the associated outflow. Following the work of Wang & Lilly (2021), we can write the basic continuity equations for gas and metals:

$$\dot{M}_{\rm gas}(t) = \Phi(t) - (1 - R)\Psi(t) - \lambda\Psi(t), \quad (3)$$

$$\dot{M}_{\rm Z}(t) = y\Psi(t) - (1 - R + \lambda)Z(t)\Psi(t) + \Phi(t)Z_0, \quad (4)$$

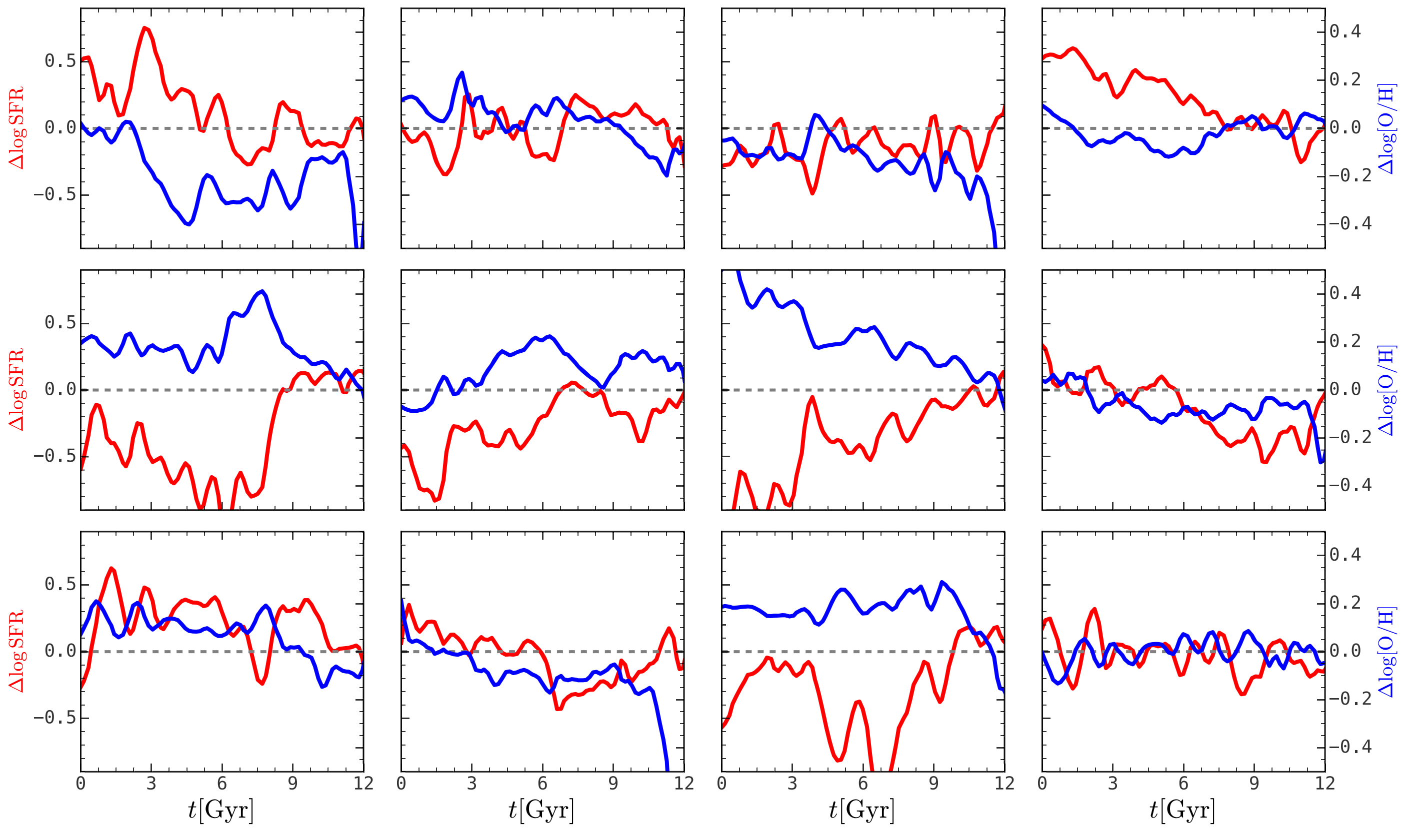

Figure 5. The evolution of the SFR and gas-phase metallicity for 12 randomly selected star-forming galaxies as a function of lookback time in the TNG50 simulation. For clear presentation, here we show the deviation from the SFMS and the median MZR. This figure clearly shows that the SFR and the gas-phase metallicity are in anticorrelation on the temporal dimension.

where $M_{\rm gas}$ is the gas mass, $M_{\rm Z}$ is the metal mass, $\Psi(t)$ is the SFR, $\Phi(t)$ is the inflow rate, Z_0 is the metallicity of inflowing gas, and y is the yield, i.e., the mass of metals returned to the interstellar medium per unit mass of formed stars. R denotes the fraction of mass formed in new stars that is subsequently returned to the interstellar medium, and λ is the mass-loading factor, i.e., the ratio between the mass outflow rate and SFR. Here we assume that the loading factor only depends on the gravitational potential, thus $M_*/R_{\rm e}$, in our toy model.

We start from the simplest case, where $\dot{M}_{\rm gas}=0$ and $\dot{M}_{\rm Z}=0$. Then we can obtain the metallicity of the system analytically, which can be written as

$$Z_{\rm gas}=Z_0+y/(1-R+\lambda). \tag{5}$$

We note that, even if the input inflow rate is time varying, one still can get the time-averaged solution in a similar form, i.e., $\langle Z_{\rm gas}\rangle = Z_0 + y/(1-R+\lambda)$ (see Figure 4 in Wang & Lilly 2021). Equation (5) says that the metallicity, $Z_{\rm gas}$, is regulated by the mass-loading factor, λ, which is directly linked to the gravitational potential. We expect that systems with deeper gravitational potential, i.e., smaller galaxy sizes, are more resistant to the stellar feedback process, thus having a lower outflow rate and lower mass-loading factor, at a given SFR. Consequently, these systems are more metal rich. This explains the correlations we saw previously in the observation and simulation, where galaxies with smaller sizes are more metal rich at a given stellar mass.

In addition, inputting the time-varying inflow rate into Equations (3) and (4), Wang & Lilly (2021) found a clear negative correlation between the SFR and $Z_{\rm gas}$ for an individual gas regulator system. It is not possible to trace the time variation for individual galaxies from the observation, while the simulations provide this important information. We therefore examine the correlation of $\Delta\log{\rm SFR}$ and $\Delta\log({\rm O/H})$ as a function of redshift for 12 TNG50 galaxies (randomly selected), as shown in Figure 5. The $\Delta\log{\rm SFR}$ and $\Delta\log({\rm O/H})$ are defined as the offsets from the SFMS and MZ relation established at corresponding redshifts. Figure 5 clearly shows negative correlations between $\Delta\log{\rm SFR}$ and $\Delta\log({\rm O/H})$ for individual galaxies, indicating that the dependence of metallicity on the SFR is indeed from the time variation of individual galaxies, at least for TNG50. Compared to gravitational potential, the SFR plays a secondary role in determining the metallicity, driven by the time-varying inflow rate.

Nonetheless, the cautious reader may have noticed some positive correlations between the $\Delta\log{\rm SFR}$ and $\Delta\log[{\rm O/H}]$, like the second panel in the bottom row. According to the toy model proposed in Wang & Lilly (2021), a time-varying SFR could only induce a negative correlation between the SFR and gas-phase metallicity, while a time-varying star formation efficiency (SFE) $\equiv {\rm SFR}/M_{\rm gas}$ could cause a positive correlation. So we inspect the SFE histories of these galaxies and indeed find an upturn of SFE for this particular galaxy (not shown here). Therefore, the rise of SFR for this galaxy from $z\approx 1$ is caused by an enhanced SFE instead of increasing inflow gas, so that the gas-phase metallicity is not diluted but, instead, enriched by the metal produced during the star formation process. Consequently, both the SFR and gas-phase metallicity arise and produce a positive correlation. Apparently, SFE also plays an important role in regulating the gas-phase metallicity of galaxies. However, calculating SFE requires estimating the total gas mass, which is quite expensive in observations and limited to a small sample of galaxies to date. In addition, the averaged SFE of a whole galaxy does not vary too much temporally (Wang & Lilly 2021), so we could ignore it in most cases.

4.3. Summary

The gas-phase metallicity of galaxies contains abundant information about astrophysical processes in galaxy formation and evolution. A common practice to decode this information is to first establish scaling relations with other galaxy properties and, then, compare them with galaxy formation models. Beyond the MZR, people start to pursue the secondary galaxy property that possesses the strongest correlation to the gas-phase metallicity, and a debate between the SFR and galaxy size arises. In this work, we use both cutting-edge observations and state-of-the-art simulations to examine the roles played by these galaxy properties in determining the gas-phase metallicity. Our findings are summarized as follows.

1. We find that, based on the MZR, the inclusion of galaxy size, $\log M_* - \beta \log R_e$, can significantly reduce the uncertainty in predicting the gas-phase metallicity, compared with using stellar mass alone, for star-forming galaxies in the MaNGA survey with three different metallicity observational indicators, despite their inherent systematics. Meanwhile, the SFR only plays a subdominant role for all three metallicity indicators. Similar conclusions are drawn in the TNG50 simulation.
2. The best-fitting coefficients for the SFR and galaxy size are $\alpha \approx 0.2$ and $\beta \approx 0.6$, respectively, for three different metallicity indicators for the MaNGA survey, while TNG50 gives $\alpha \approx 0.5$ and $\beta \approx 1.0$.
3. Through performing similar analyses at different redshifts in TNG50, we find that the SFR plays an increasingly important role in predicting metallicity at high z, and the best-fitting value of α also increases with redshift. On the other side, the best-fitting value of β is always ≈ 1 from $z \approx 0$ to $z \approx 5$.
4. Based on the statistical analysis of the relationship among the gas-phase metallicity, galaxy size, and SFR, we speculate that the SFR modulates metallicity on the temporal dimension, synchronized to the gas inflow process, while galaxy size regulates metallicity on the spatial dimension through affecting the gravitational potential and the mass-loading factor.

Our analysis here mainly focuses on statistical analysis in our local Universe. Nevertheless, with the advent of high-z galaxy surveys, we expect to investigate the statistical relationship between metallicity and other galaxy properties at cosmic noon to understand the underlying astrophysical process and even directly inspect the metal exchange between galaxies and their surrounding medium (Zhang et al. 2023), which is more prevalent in the early Universe.

Acknowledgments

The authors thank the anonymous referee for their helpful comments that improved the quality of this Letter. This work is supported by the National Science Foundation of China (NSFC) grant Nos. 12233008, 12125301, 12192220, and 12192222; the National Key R&D Program of China (2023YFA1608100); and the science research grants from the China Manned Space Project with grant No. CMS-CSST-2021-A07. The authors gratefully acknowledge the support of Cyrus Chun Ying Tang Foundations.

Appendix
Gravitational Potential

Here we examine whether the M_*/R_e can be a good indicator of the gravitational potential of the whole system, including both baryonic and dark matter particles. We randomly select 100 galaxies that span a wide range of stellar mass for this test.

We calculate the gravitational potential at the radius of R_e in the following way. For simplicity, we calculate the mean potential of a sphere with the radius of R_e centered at the galactic center. In this case, the mean potential at this sphere for a given particle (with mass of M_{par}) within the sphere can be expressed as $-GM_{par}/R_e$, and this value changes to be $-GM_{par}/r$ for a particle out of the sphere, where r is the distance to the galaxy center. Then we sum over all the particles to obtain the mean gravitational potential of individual galaxies.

Figure 6 shows the correlation between the gravitational potential at R_e calculated above and the M_*/R_e. Interestingly, we do find the two show a tight relation, with a correlation coefficient of 0.86. This confirms that M_*/R_e indeed can be a good tracer as the overall gravitational potential of galaxies.

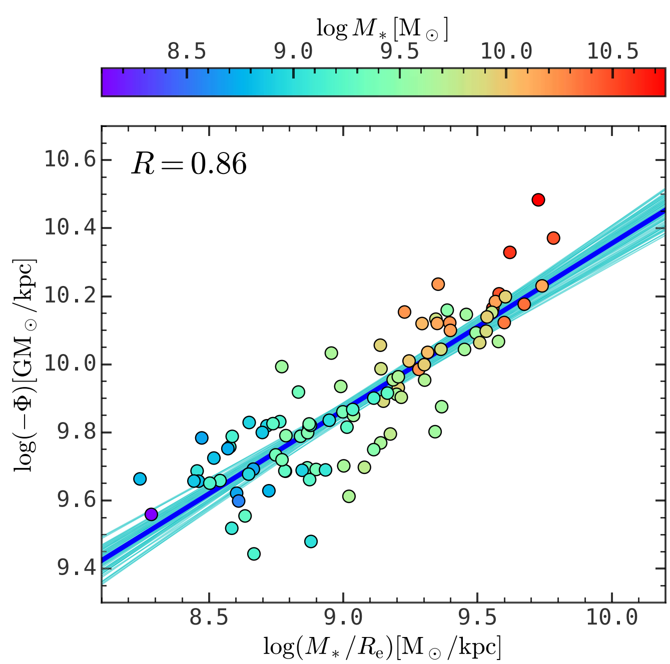

Figure 6. The gravitational potential vs. the M_*/R_e for a randomly selected a sample of 100 galaxies. The blue line shows the linear fitting for the two quantities with the correlation coefficient of 0.86, indicating strong correlations between the two.

ORCID iDs

Chengyu Ma https://orcid.org/0009-0006-7343-8013
Kai Wang https://orcid.org/0000-0002-3775-0484
Enci Wang https://orcid.org/0000-0003-1588-9394
Yingjie Peng https://orcid.org/0000-0003-0939-9671
Haochen Jiang https://orcid.org/0009-0006-1483-4323
Xu Kong https://orcid.org/0000-0002-7660-2273

References

Abdurro'uf, Accetta, K., Aerts, C., et al. 2022, ApJS, 259, 35
Barone, T. M., D'Eugenio, F., Colless, M., & Scott, N. 2020, ApJ, 898, 62
Bassini, L., Feldmann, R., Gensior, J., et al. 2024, MNRAS, 532, L14
Belfiore, F., Vincenzo, F., Maiolino, R., & Matteucci, F. 2019, MNRAS, 487, 456
Bouché, N., Dekel, A., Genzel, R., et al. 2010, ApJ, 718, 1001
Brooks, A. M., Governato, F., Booth, C. M., et al. 2007, ApJL, 655, L17
Bundy, K., Bershady, M. A., Law, D. R., et al. 2015, ApJ, 798, 7
Calura, F., Pipino, A., Chiappini, C., Matteucci, F., & Maiolino, R. 2009, A&A, 504, 373
Cappellari, M. 2023, MNRAS, 526, 3273
Cirasuolo, M., Afonso, J., Carollo, M., et al. 2014, Proc. SPIE, 9147, 91470N
Cresci, G., Mannucci, F., & Curti, M. 2019, A&A, 627, A42
Curti, M., Mannucci, F., Cresci, G., & Maiolino, R. 2020, MNRAS, 491, 944
Curti, M., Maiolino, R., Curtis-Lake, E., et al. 2024, A&A, 684, A75
Davé, R., Finlator, K., & Oppenheimer, B. D. 2011, MNRAS, 416, 1354
D'Eugenio, F., Colless, M., Groves, B., Bian, F., & Barone, T. M. 2018, MNRAS, 479, 1807
Donnari, M., Pillepich, A., Nelson, D., et al. 2019, MNRAS, 485, 4817
Dopita, M. A., Kewley, L. J., Sutherland, R. S., & Nicholls, D. C. 2016, Ap&SS, 361, 61
Dopita, M. A., Sutherland, R. S., Nicholls, D. C., Kewley, L. J., & Vogt, F. P. A. 2013, ApJS, 208, 10
Easeman, B., Schady, P., Wuyts, S., & Yates, R. M. 2024, MNRAS, 527, 5484
Ellison, S. L., Patton, D. R., Simard, L., & McConnachie, A. W. 2008, ApJ, 672, L107
Finlator, K., & Davé, R. 2008, MNRAS, 385, 2181
Garcia, A. M., Torrey, P., Grasha, K., et al. 2024, MNRAS, 529, 3342
Gunn, J. E., Siegmund, W. A., Mannery, E. J., et al. 2006, AJ, 131, 2332
Huang, C., Zou, H., Kong, X., et al. 2019, ApJ, 886, 31
Kewley, L. J., & Dopita, M. A. 2002, ApJS, 142, 35
Lara-López, M. A., Cepa, J., Bongiovanni, A., et al. 2010, A&A, 521, L53
Larson, R. B. 1974, MNRAS, 169, 229
Lequeux, J., Peimbert, M., Rayo, J. F., Serrano, A., & Torres-Peimbert, S. 1979, A&A, 500, 145
Lilly, S. J., Carollo, C. M., Pipino, A., Renzini, A., & Peng, Y. 2013, ApJ, 772, 119
Ma, H.-C., Du, M., Ho, L. C., Sheng, M.-j., & Liao, S. 2024, arXiv:2404.10432
Maier, C., Lilly, S. J., Carollo, C. M., et al. 2006, ApJ, 639, 858
Maiolino, R., Nagao, T., Grazian, A., et al. 2008, A&A, 488, 463
Maiolino, R., Cirasuolo, M., Afonso, J., et al. 2020, Msngr, 180, 24
Mannucci, F., Cresci, G., Maiolino, R., Marconi, A., & Gnerucci, A. 2010, MNRAS, 408, 2115
Nakajima, K., Ouchi, M., Shimasaku, K., et al. 2012, ApJ, 745, 12
Nelson, D., Pillepich, A., Springel, V., et al. 2018, MNRAS, 475, 624
Peng, Y.-j., & Maiolino, R. 2014, MNRAS, 443, 3643
Pérez-Díaz, B., Pérez-Montero, E., Fernández-Ontiveros, J. A., Vílchez, J. M., & Amorín, R. 2024, NatAs, 8, 368
Pillepich, A., Springel, V., Nelson, D., et al. 2018, MNRAS, 473, 4077
Pilyugin, L. S., & Grebel, E. K. 2016, MNRAS, 457, 3678
Richard, J., Jones, T., Ellis, R., et al. 2011, MNRAS, 413, 643
Salim, S., Boquien, M., & Lee, J. C. 2018, ApJ, 859, 11
Salim, S., Lee, J. C., Ly, C., et al. 2014, ApJ, 797, 126
Sánchez Almeida, J., & Dalla Vecchia, C. 2018, ApJ, 859, 109
Sánchez-Menguiano, L., Sánchez, S. F., Sánchez Almeida, J., & Muñoz-Tuñón, C. 2024a, A&A, 682, L11
Sánchez-Menguiano, L., Sánchez Almeida, J., Sánchez, S. F., & Muñoz-Tuñón, C. 2024b, A&A, 681, A121
Savaglio, S., Glazebrook, K., Le Borgne, D., et al. 2005, ApJ, 635, 260
Schaye, J., Dalla Vecchia, C., Booth, C. M., et al. 2010, MNRAS, 402, 1536
Schaye, J., Crain, R. A., Bower, R. G., et al. 2015, MNRAS, 446, 521
Smee, S. A., Gunn, J. E., Uomoto, A., et al. 2013, AJ, 146, 32
Springel, V., White, S. D. M., Jenkins, A., et al. 2005, Natur, 435, 629
Stoughton, C., Lupton, R. H., Bernardi, M., et al. 2002, AJ, 123, 485
Takada, M., Ellis, R. S., Chiba, M., et al. 2014, PASJ, 66, R1
Tremonti, C. A., Heckman, T. M., Kauffmann, G., et al. 2004, ApJ, 613, 898
Vaughan, S. P., Barone, T. M., Croom, S. M., et al. 2022, MNRAS, 516, 2971
Wang, E., & Lilly, S. J. 2021, ApJ, 910, 137
Wang, E., & Lilly, S. J. 2022, ApJ, 929, 95
Wang, E., Lilly, S. J., Pezzulli, G., & Matthee, J. 2019, ApJ, 877, 132
Wang, K., Peng, Y., & Chen, Y. 2023a, MNRAS, 523, 1268
Wang, K., Wang, X., & Chen, Y. 2023b, ApJ, 951, 66
Woo, J., Dekel, A., Faber, S. M., et al. 2013, MNRAS, 428, 3306
Zhang, K., Yan, R., Bundy, K., et al. 2017, MNRAS, 466, 3217
Zhang, S., Cai, Z., Xu, D., et al. 2023, Sci, 380, 494